

## Microwave hysteretic losses in $\text{YBa}_2\text{Cu}_3\text{O}_{7-x}$ and NbN thin films

P. P. Nguyen

*Department of Physics, Massachusetts Institute of Technology, Cambridge Massachusetts 02139  
and Rome Laboratory, USAF, Hanscom AFB, Massachusetts 01731*

D. E. Oates

*Lincoln Laboratory, Massachusetts Institute of Technology, Lexington Massachusetts 02173*

G. Dresselhaus

*Francis Bitter Magnet Laboratory, Massachusetts Institute of Technology, Cambridge, Massachusetts 02139  
and Rome Laboratory, USAF, Hanscom AFB, Massachusetts 01731*

M. S. Dresselhaus

*Department of Electrical Engineering and Computer Science and Department of Physics,  
Massachusetts Institute of Technology, Cambridge, Massachusetts 02139*

A. C. Anderson

*Lincoln Laboratory, Massachusetts Institute of Technology, Lexington, Massachusetts 02173*

(Received 17 August 1994)

Measurements of the nonlinear surface impedance of high-quality epitaxial YBCO and granular NbN films as a function of temperature (4.2–91 K) and frequency (1–13 GHz) are presented. The microwave-field-dependent surface impedance  $Z_s(H_{\text{rf}})$  for both YBCO and NbN films increases quadratically with increasing  $H_{\text{rf}}$  in the low- and intermediate-rf-field region ( $H_{\text{rf}} < 50$  Oe for YBCO at 77 K and for NbN at 13.4 K). In the high-rf-field region,  $Z_s(H_{\text{rf}})$  changes to a different functional dependence on  $H_{\text{rf}}$ . Through the use of a modified Bean critical-state model, the results for the high-rf-field region are explained quantitatively by hysteresis losses due to penetration of microwave vortices. The value of the microwave-vortex penetration field  $H_p(T)$  for YBCO thin films, which is nearly frequency independent, is low compared with the dc lower critical fields. The critical-current density values obtained from fits to the hysteresis model are consistent with those measured via dc transport.

### I. INTRODUCTION

Microwave measurements provide a sensitive probe of the superconducting state of high-temperature superconductors. From the measured surface impedance  $Z_s = R_s + jX_s$ , losses and the London penetration depth  $\lambda$  can be extracted directly from the surface resistance  $R_s$  and surface reactance  $X_s$ . At very low microwave powers ( $H_{\text{rf}} < 1$  Oe for YBCO superconducting films, where  $H_{\text{rf}}$ , the peak rf magnetic field at the edges of a stripline resonator, is generated by the microwave current),  $R_s$  directly results from the presence of quasiparticles and defects in the grains, and from grain boundaries between the grains.<sup>1</sup> Measurement of  $\lambda$  can reveal the symmetry of the superconducting condensate.<sup>2</sup> The behavior of  $\lambda$  in an externally applied dc magnetic field also allows an accurate determination of the lower critical field  $H_{c1}$ .<sup>3,4</sup>

In the low- and intermediate-microwave-power regime (where  $H_{\text{rf}} < 50$  Oe at 77 K for a typical YBCO thin film),  $Z_s$  has been observed to be nonlinear; i.e.,  $Z_s$  changes with the microwave power.<sup>1,5–7</sup> The power dependence of  $Z_s$  in the low- and intermediate-field regime has been quantitatively explained in an earlier publication by an extended microwave-power-dependent coupled-grain model that we developed,<sup>1</sup> which treats

the superconductor as a network of superconducting grains connected by grain boundaries acting as resistively shunted Josephson junctions.<sup>8–10</sup> The low- and intermediate-field regime corresponds to the Meissner state of the coupled-grain network. According to this power-dependent coupled-grain model, the  $Z_s$  of the superconducting junction network is nonlinear because the imaginary part of the junctions's impedance varies with input power.

As the microwave power is increased into the high-power regime ( $H_{\text{rf}} > 50$  Oe at 77 K for a typical YBCO thin film),  $Z_s$  becomes more strongly nonlinear than in the intermediate-power regime; i.e.,  $R_s$  and  $\lambda$  both increase more rapidly.<sup>1</sup> Such nonlinear effects have not been well understood in the high-power regime despite the interesting physics involved and the obvious importance of this nonlinear behavior of  $Z_s$  to film and device makers.<sup>11,12</sup> This paper presents measurements of the losses at high microwave powers and explains them with a modified Bean critical-state model.

### II. EXPERIMENTAL TECHNIQUES

The seven measured YBCO films were deposited *in situ* onto  $\text{LaAlO}_3$  substrates by off-axis sputtering,<sup>13</sup>

TABLE I. Parameters of films.

Film	Sample	Thickness [ $\mu\text{m}$ ]	$\lambda(0)$ [ $\mu\text{m}$ ] <sup>a</sup>	$T_c$ [K] <sup>a</sup>	$H_p(T)$ [Oe] <sup>b</sup>	$J_c^P(T)$ [A/cm <sup>2</sup> ] <sup>b</sup>
YBCO						
Off-axis	1	0.30	0.17	86.4	190 (11 K)	$1.5 \times 10^7$ (11 K)
Off-axis	2	0.30	0.22	89.5	37 (77 K)	$5.3 \times 10^6$ (77 K)
Off-axis	3	0.30	0.27	89.6	27 (77 K)	$1.0 \times 10^6$ (77 K)
Cylindrical	4	0.80	0.23	87	102 (77 K)	$2.8 \times 10^6$ (77 K)
Cylindrical	5	0.20	0.22	88	189 (6 K)	$1.8 \times 10^7$ (6 K)
Pulsed laser	6	0.10	0.16	91	145 (4.3 K)	$5.5 \times 10^7$ (4.3 K)
Off-axis	7	0.20	0.17	90	17 (77 K)	$4.8 \times 10^6$ (77 K)
NbN						
On-axis	NbN1	0.80	0.39	15.3	42 (13.4 K)	$1.2 \times 10^5$ (13.4 K)
On-axis	NbN2	0.80	0.39	15.9		

<sup>a</sup>Obtained by method described by Sheen *et al.* (Ref. 21).

<sup>b</sup>Pinning critical-current density  $J_c^P$  and vortex-penetration field  $H_p$  are obtained from fits to the fundamental modes using the modified Bean model; see text.

inverted-cylindrical-magnetron sputtering,<sup>14</sup> and pulsed laser deposition.<sup>15</sup> The transition temperatures  $T_c$  obtained via microwave  $Z_s$  measurements range from 87 K to 91 K. The dc critical-current densities that we measured for the YBCO films exceed  $10^7 \text{ A/cm}^2$  at 4.2 K. The low-rf-field  $R_s$  is comparable to that of other high-quality films reported in the literature;<sup>16</sup> e.g., for sample 7 in Table I,  $R_s$  at 1.5 GHz is  $1.3 \mu\Omega$  at 19 K and  $12 \mu\Omega$  at 77 K. Two polycrystalline NbN films (Table I) deposited on sapphire substrates by planar on-axis dc magnetron sputtering of a pure Nb target in an argon-nitrogen mixture were also measured for comparison.<sup>17</sup> NbN was chosen because it is a conventional superconductor whose properties are similar to high- $T_c$  materials: large  $T_c$ , high upper critical field  $H_{c2}$ , high critical-current density, strongly type II (i.e., the Ginzburg-Landau parameter  $\kappa \gg 1/\sqrt{2}$ ), etc.<sup>18,19</sup>

After being patterned with standard photolithography, the YBCO and NbN films were etched with 0.25% phosphoric acid and reactive ions in a CFC plasma, respectively, and assembled into stripline resonators. From the measured  $Q$  and resonant frequency  $f_0$ , we extract  $R_s$  and  $\lambda$ . The details of the resonators, measurements, and determination of  $Z_s$  from the measured quantities were described previously.<sup>1,20,21</sup> At low rf currents (linear  $Z_s$ ),  $R_s$ ,  $\lambda$ , and  $H_{rf}$  can be numerically calculated.<sup>21</sup> At high rf currents, as the complex resistivity of the material is no longer uniform,  $R_s$  and  $\lambda$  are not well defined, and  $H_{rf}$  has to be corrected to account for the change in the rf-current distribution, especially if vortices are assumed to enter the films and the current distribution is no longer that of the Meissner state. We will continue, however, to employ these parameters in their average forms as described by Nguyen *et al.*<sup>1</sup> because they are useful and intuitive parameters. The corresponding well-defined parameters would be the unloaded quality factor  $Q_u$ , the resonant frequency  $f_0$ , and the rf current on the standing-wave peaks  $I_{rf}$ . We define our average parameters as follows:

$$1/R_s \propto Q_u, \quad \Delta\lambda \propto \Delta f_0, \quad H_{rf} \propto I_{rf},$$

with the same proportionality constants as those in the low-rf-current situation.<sup>1</sup> The  $Q_u$ ,  $f_0$ , and  $I_{rf}$  are not used in this paper because they are not fundamental parameters; they depend on the geometry of the measurements. It is important, however, to keep in mind that the quantities  $R_s$ ,  $\lambda$ , and  $H_{rf}$  used in this work are meaningful only as long as they are regarded as alternative expressions of the  $Q_u$ ,  $f_0$ , and  $I_{rf}$ . These alternative expressions, of course, revert fully to their well-defined usual meanings at low rf powers.

### III. EXPERIMENTAL RESULTS

Figure 1 shows the measured  $R_s$  and  $\lambda$  as functions of  $H_{rf}$  for sample 1. Similar results are obtained for the other films. The behavior of both  $R_s$  and  $\lambda$  is qualita-

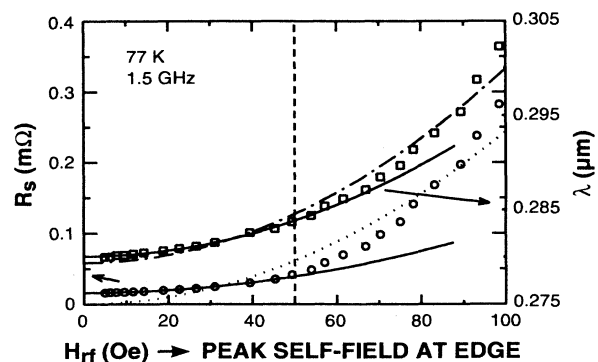


FIG. 1. The measured  $R_s$  ( $\circ$ ) and  $\lambda$  ( $\square$ ) vs  $H_{rf}$  for YBCO sample 1 at 77.4 K and 1.5 GHz. The vertical dashed line at 50 Oe marks the approximate place where  $R_s$  and  $\lambda$  deviate noticeably from a quadratic dependence on  $H_{rf}$ . The solid lines are the best quadratic fits of the power-dependent coupled-grain model (Ref. 1) to the low- and intermediate-field region ( $< 50$  Oe). The dashed lines are the best general quadratic fits for the entire rf-field range both below and above 50 Oe to demonstrate the nonquadratic behavior of  $R_s$  and  $\lambda$ .

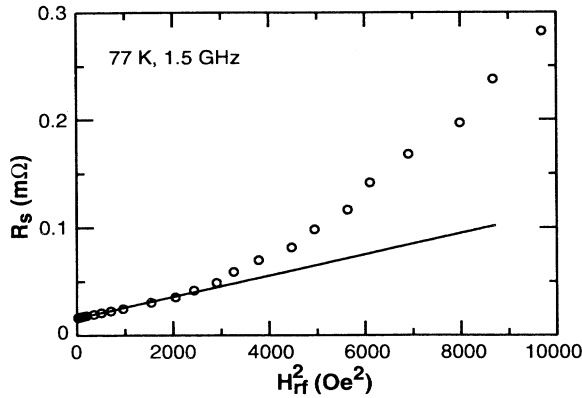


FIG. 2. Surface resistance  $R_s$  vs  $H_{rf}^2$  for sample 1 at the same temperature (77.4 K) and frequency (1.5 GHz) as in Fig. 1. In the low- and intermediate-field region, the data follow a straight line as the linear fit (solid line) shows.

tively different for the low- and intermediate-rf-field and high-rf-field regions. For the low- and intermediate-field region ( $H_{rf} < 50$  Oe for sample 1),  $R_s$  and  $\lambda$  increase quadratically in  $H_{rf}$ , as discussed in a previous paper:<sup>1</sup>

$$R_s = R_s(0)[1 + b_R H_{rf}^2] \quad (1)$$

and

$$\lambda = \lambda(0)[1 + b_\lambda H_{rf}^2], \quad (2)$$

where  $b_R$  and  $b_\lambda$  are quadratic coefficients. In the high-rf-field region ( $> 50$  Oe for sample 1), both  $R_s$  and  $\lambda$  increase faster than the quadratic dependences observed in the low- and intermediate-rf-field region. The dashed lines in Fig. 1 are the best quadratic fits to the *entire field range* of  $R_s(H_{rf})$  and  $\lambda(H_{rf})$ . The noticeably large deviation of the fits from the data indicates that  $R_s$  and  $\lambda$  are not well described by the simple quadratic functions of Eq. (1) and Eq. (2). Figure 2 plots  $R_s$  vs  $H_{rf}^2$  to emphasize the quadratic behavior in the low- and intermediate-field regime. It is more illuminating to plot  $\Delta R_s(H_{rf})$  vs  $\Delta\lambda(H_{rf})$ , as shown in Fig. 3 for sample 1 at the same temperature and resonant frequency as in Fig. 1.  $\Delta R_s(H_{rf})$  and  $\Delta\lambda(H_{rf})$  are the changes in  $R_s$  and  $\lambda$ , respectively, induced by the increasing rf magnetic field. The inset shows the full field range. As seen in the figure, the large difference of the slope between the low- and intermediate-field and high-field regions suggests two different kinds of loss mechanisms governing the two regions.

For comparison,  $R_s$  and  $\lambda$  as functions of  $H_{rf}$  for NbN are presented in Fig. 4 at approximately the same reduced temperature  $T/T_c = 13.4/15.3 \approx 77/87$  as for YBCO sample 1 in Fig. 1. The quadratic dependence on  $H_{rf}$  is again observed in the low- and intermediate-rf-field region ( $< 48$  Oe). In the high-rf-field region, the deviation from quadratic dependence is much more drastic than that in YBCO, making the distinction between the two regions much more obvious. (The difference in the magnitudes of the deviation in the high-rf-field regime between YBCO and NbN can be explained by the dif-

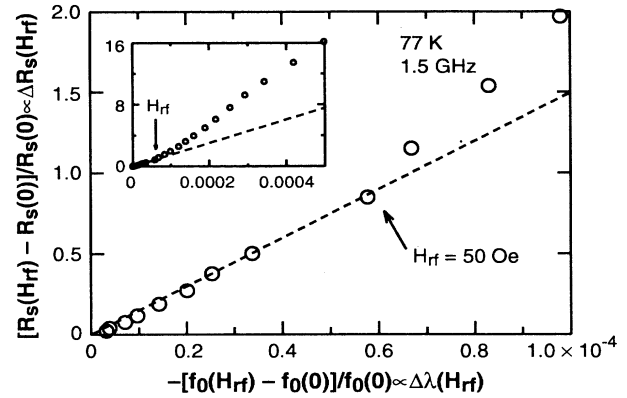


FIG. 3. The rf-field-induced changes  $\Delta R_s(H_{rf})$  vs  $\Delta\lambda(H_{rf})$  for sample 1 at the same temperature and resonant frequency as in Fig. 1. The inset shows the entire field range whereas the main plot magnifies the transition region (around 50 Oe) between the low- and intermediate-field regime and the high-field regime. The slope is observed to change noticeably upon crossing from one region to the next, signifying the appearance of new loss mechanisms.

ferent magnitudes of their critical-current densities, as discussed later.) Figure 5 plots the fractional change of  $R_s$  vs  $\lambda$  as induced by the rf current. Again, as for YBCO films, a large change in the slope is observed as the data cross from the low- and intermediate-field region to the high-field region.

The low- and intermediate-field region has been quantitatively explained by the power-dependent coupled-grain

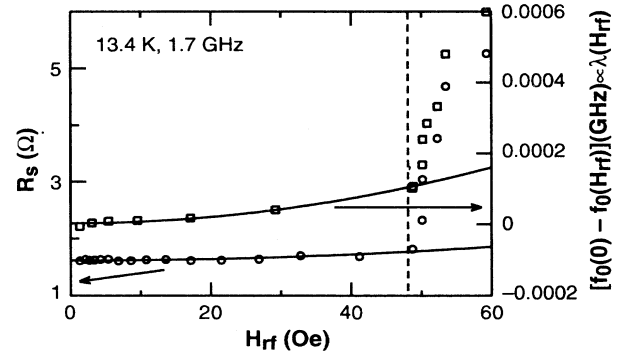


FIG. 4. The measured  $R_s$  ( $\circ$ ) and  $\lambda$  ( $\square$ ) vs  $H_{rf}$  for NbN sample 1 at similar reduced temperature  $T/T_c = 13.4$  K/15.3 K as for YBCO sample 1 in Fig. 1 with  $T/T_c = 77$  K/87 K. The vertical dashed line at about 49 Oe marks the place where  $R_s$  and  $\lambda$  start to deviate noticeably from a quadratic dependence on  $H_{rf}$ . The solid lines are the best quadratic fits to the power-dependent coupled-grain model (Ref. 1) for the low- and intermediate-field region ( $< 49$  Oe). Note that the distinction between the low- and intermediate-field and the high-field regions is much clearer for NbN than for YBCO films, since the slopes of  $R_s$  and  $\lambda$  for NbN change much more rapidly upon crossing into the high-field region.

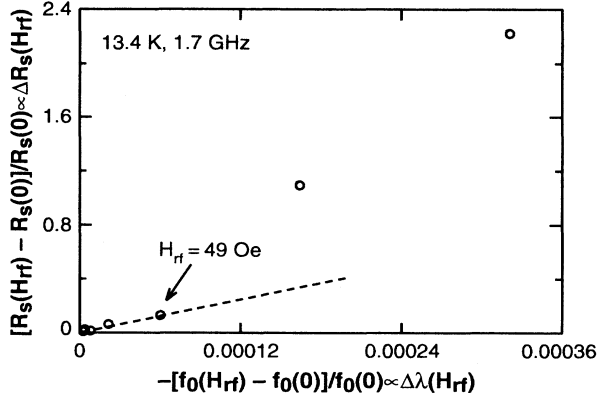


FIG. 5. The rf-field-induced changes  $\Delta R_s(H_{rf})$  vs  $\Delta\lambda(H_{rf})$  for NbN sample 1 at the same temperature and resonant frequency as in Fig. 4. The slope changes noticeably upon crossing the same field value, 49 Oe, as in Fig. 4, signifying the appearance of new loss mechanisms.

model in the Meissner state.<sup>1</sup> It is the focus of this paper to explore the high-rf-field region. We propose that in the high-field region, above a certain vortex-penetration field  $H_p$ , rf vortices form and enter the sample, introducing vortex-loss mechanisms. The superconducting film is treated as an effective continuous medium by averaging over the grains, defects, and grain boundaries. The field  $H_p$  is thus the microwave equivalent of the dc lower critical field  $H_{c1}$ . Note that in the high-rf-field regime, the losses described by the power-dependent coupled-grain model are still present. These losses, referred to hereafter as Meissner losses, exist simultaneously with the added vortex-loss mechanisms, because the Meissner shielding surface current persists even after vortex penetration.<sup>22,23</sup> Furthermore, in the stripline geometry with  $H_{rf}$  not much larger than  $H_p$ , vortices enter only the sections of the line around the peaks of the resonant standing wave (see Fig. 6). Part (a) of Fig. 6 shows a thin strip with microwave current  $I_{rf} \propto H_{rf}$  flowing along the length. Part (b) shows the amplitude of  $I_{rf} \propto H_{rf}$  along the length of the strip. Recall that  $H_{rf}$  is the peak rf field at the edges of the maxima of the resonant standing wave and is a function only of the coordinate  $z$  along the length of the line. The sinusoidal solid and dashed lines represent the standing waves of the first and second resonant modes, respectively. The positions of the intersection of the first-mode curve with the  $H_p$  horizontal line are also given. From Fig. 6, we see that for a maximum field  $H_{rf}$  not much larger than  $H_p$ , the rf fields in most areas of the stripline remain less than  $H_p$ . These areas hence are in the Meissner state. Thus

$$R_s = R_s^M + R_s^B, \quad (3)$$

where  $R_s^M$  and  $R_s^B$  correspond to Meissner and vortex hysteretic losses, respectively.  $R_s^M$  can be approximated above  $H_p$  by the power-dependent coupled-grain model.<sup>1</sup> Since hysteretic losses due to rf vortices are much larger than Meissner losses at sufficiently high rf fields,  $R_s^B$  can

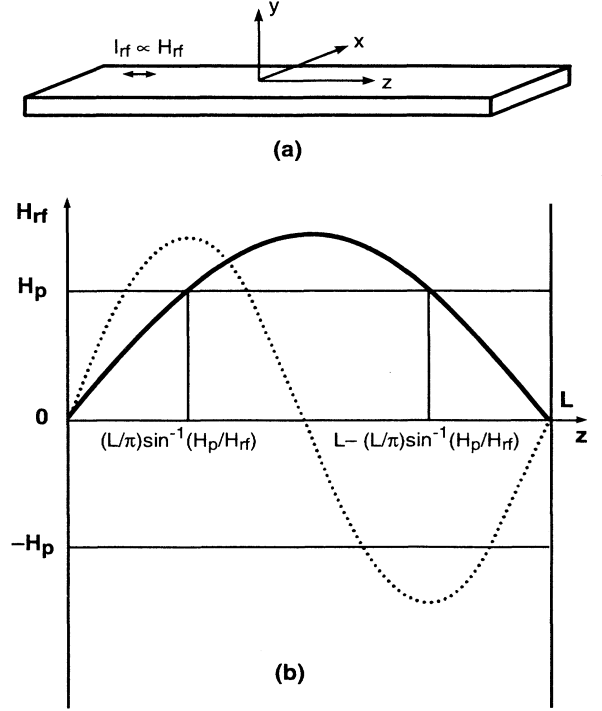


FIG. 6. (a) Thin-strip geometry with microwave current  $I_{rf} \propto H_{rf}$  flowing along the length. (b) Amplitude of  $H_{rf}$  (or  $I_{rf}$ ) along the length of the strip. The sinusoidal solid and dashed lines represent the first and second standing-wave resonant modes, respectively. The positions of the intersection of the first-mode curve with the  $H_p$  horizontal line are also shown.

be deduced quite accurately using Eq. (3). In the next section, we calculate the unloaded  $Q_u$  of the stripline resonator using a critical-state model. The calculated  $Q_u$  will then be inverted to give the effective surface resistance  $R_s^B$  to compare with the measurements.

#### IV. ANALYSIS

The critical-state model is used to calculate the hysteretic losses at high rf fields. As the model does not distinguish between Abrikosov and Josephson vortices, we treat the films as an effective continuous medium, averaging over grains, defects, and grain boundaries. Using the Bean critical-state model in which the lower critical field  $H_{c1}$  is assumed to be 0, Norris calculated hysteretic losses<sup>24</sup> incurred in a thin strip of width much greater than its thickness by a low-frequency  $f < 1$  kHz current  $I(t)$  with amplitude  $I_0$ . The emf (per unit length) induced in the strip is  $E(x) = \partial\phi(x)/\partial t$  where  $x$  refers to the coordinate (Fig. 6) along the width  $2a$  of the strip, and the flux  $\phi(x) = \mu_0 \int_0^x H(s) ds$  where  $\mu_0$  is the permeability of free space. In each cycle, the energy dissipated  $U_{\text{cycle}}$  equals

$$U_{\text{cycle}} = \int_0^{1/f} dt \int_{-a}^a j(x) E(x) dx, \quad (4)$$

where conformal mapping gives the sheet current  $j$  which is the current density integrated over the sample thickness.<sup>24</sup> The dissipated power per unit length  $\mathcal{P}$  due to hysteresis is found by Norris<sup>24</sup> to be

$$\mathcal{P} = \frac{f\mu_0 I_c^2}{\pi} [(1-F)\ln(1-F) + (1+F)\ln(1+F) - F^2], \quad (5)$$

where  $F = (I_0/I_c)$  and  $I_c = J_c^P A$  with  $J_c^P$  the critical-current density arising from vortex pinning (i.e.,  $J_c^P$  is determined by the balance between the Lorentz and pinning forces.<sup>25,26</sup>  $J_c^P \propto U$  where  $U$  is the vortex pinning potential) and  $A$  the cross-sectional area of the strip. Equation (5) includes both the vortex-motion and vortex-annihilation losses.<sup>27</sup> For  $I_0 \ll I_c$ , Eq. (5) reduces to

$$\mathcal{P} \simeq \frac{f\mu_0}{\pi I_c^2} I_0^4. \quad (6)$$

Because of the thin-strip geometry, the hysteretic losses grow initially with the fourth power of the amplitude  $I_0$ , instead of the well-known third power derived for a semi-infinite superconducting slab.<sup>28</sup> From Eq. (6), as  $I_0 \rightarrow 0$ ,  $R_s \propto \mathcal{P}/I_0^2$  goes to 0 as  $I_0^2$  for the thin-film geometry. In contrast, as  $I_0 \rightarrow 0$ ,  $R_s \propto I_0$  for an infinite slab.

Since there was no limit imposed on  $f$  in the derivation, Eq. (5) should apply equally well at microwave frequencies.<sup>5</sup> Similarly, because the dimension along the film thickness does not enter Norris's conformal mapping formalism, Eq. (5) can be used for the anisotropic high- $T_c$  superconductors. The bulk lower critical field  $H_{c1}$ , below which the superconductor is in the Meissner state (no vortices), however, is assumed to be zero in both Bean's model and Norris's calculation. The assumption of vortex penetration at arbitrarily small magnetic fields, whether externally applied or induced by traversing current, is invalid for a real superconductor (see the Appendix). For a magnetic field much larger than  $H_{c1}$ , the assumption  $H_{c1} \equiv 0$  gives a good approximation. For fields around  $H_{c1}$ , however, this assumption breaks down. To account for  $H_{c1} > 0$ , we need to apply the modified Bean model<sup>22,23</sup> to Norris's calculation. From the modified Bean model, no hysteretic losses are present for  $H_0 < H_{c1}$  where  $H_0(I_0)$  induced by  $I_0$  is the peak magnetic field at the edge of the strip, since there are no vortices penetrating the superconductor. For  $H_0 > H_{c1}$ ,  $H_0$  is replaced by  $H_0 - H_{c1}$ . The vortex-penetration field  $H_{c1}$  is included for  $H_0 > H_{c1}$  because the equilibrium magnetization from the Meissner shielding surface current continues to exist even after vortex penetration.<sup>22,23</sup> With the above modifications, applying Norris's calculation to the stripline geometry, we obtain hysteretic power losses per unit length for resonant mode  $n$ , for  $I_p < I_{rf} \ll I_c$ :

$$\mathcal{P}^B \simeq \frac{nf_{0,m1}\mu_0}{\pi I_c^2} \int_0^L \left( I_{rf} \sin \frac{\pi z}{L} - I_p \right)^4 \frac{dz}{L}, \quad (7)$$

where the rf current amplitude  $I_{rf}$  replaces  $I_0$  in Eq. (6),  $I_p$  is the total peak rf current which produces a peak

rf field  $H_p$  with vortex-penetration field  $H_p$  in place of  $H_{c1}$ ,  $n$  is the resonant mode number,  $f_{0,m1}$  the fundamental frequency, and  $L$  the length of the center line of the stripline resonator. The prime restricts the integral to the portions along the length of the stripline resonator (Fig. 6) in which  $I_{rf} \sin(\pi z/L)$  is larger than  $I_p$ . We neglected the small contribution from the ground planes ( $\ll 10\%$ ). Furthermore, the standing wave of the current  $I_{rf}(z)$  is assumed to remain sinusoidal along the stripline, because the total inductance per unit length which determines the current distribution along the strip length is changed little upon flux penetration.<sup>1</sup> (The kinetic inductance changes upon flux penetration, but this change is still very small compared with the nearly unchanged geometric inductance which is more than two orders of magnitude larger.<sup>21</sup>) From the hysteretic quality factor  $Q^B = 2\pi f \mathcal{E}/\mathcal{P}^B$  where  $\mathcal{E} = \mathcal{L}I_{rf}^2$  is the total stored energy per unit length and  $\mathcal{L}$  the total inductance per unit length of the stripline, the microwave surface resistance due to hysteretic losses can be derived:

$$R_s^B \simeq \frac{nf_{0,m1}\Gamma\mu_0}{12\pi^2 \mathcal{L}I_c^2 C \Delta} F(H_{rf}), \quad (8)$$

with

$$F(H_{rf}) \equiv \int_{\frac{L}{\pi} \arcsin(\frac{H_p}{H_{rf}}}^{L - \frac{L}{\pi} \arcsin(\frac{H_p}{H_{rf}})} \left( H_{rf} \sin \frac{\pi z}{L} - H_p \right)^4 \frac{dz}{H_{rf}^2 \frac{dz}{L}}, \quad (9)$$

where  $H_{rf}^2 = CI_{rf}^2$  with  $C$  a function of temperature only,<sup>1</sup>  $\Gamma = 0.41 \Omega/\text{GHz}$  is a geometrical factor, and  $\Delta(\lambda(T)/\text{thickness})$  is a correction factor for finite film thickness.<sup>20</sup> Note that  $R_s^B \propto f$ , as expected for hysteretic losses, and  $R_s^B \propto 1/(J_c^P)^2$  where  $J_c^P \equiv I_c/A$ . Recall that  $J_c^P$  or  $I_c$  refers to the current density or the corresponding total current determined by vortex pinnings as discussed in the next section. Equation (9) can be integrated exactly,

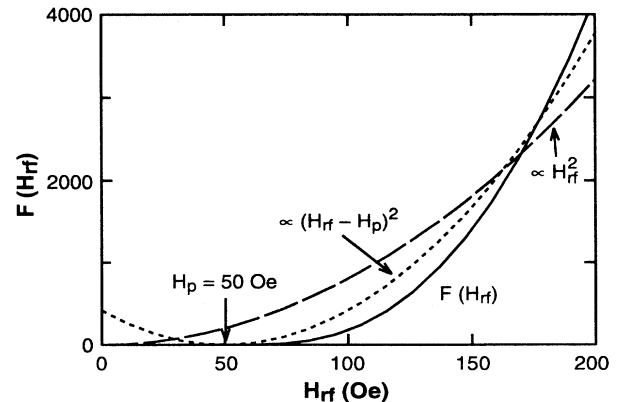


FIG. 7. Function  $F(H_{rf})$  vs  $H_{rf}$  with  $H_p \equiv 50$  Oe. For comparison, two quadratic curves  $\propto H_{rf}^2$  (dashed line) and  $\propto (H_{rf} - H_p)^2$  (dotted line) are shown to emphasize the non-quadratic behavior of  $F(H_{rf})$  around  $H_p$ .

$$F(H_{\text{rf}}) = \frac{H_p^4}{24\pi H_{\text{rf}}^2} \{ [24\pi + 72\pi(H_{\text{rf}}/H_p)^2 + 9\pi(H_{\text{rf}}/H_p)^4] - [100 + 110(H_{\text{rf}}/H_p)^2] \sqrt{(H_{\text{rf}}/H_p)^2 - 1} - [48 + 144(H_{\text{rf}}/H_p)^2 + 18(H_{\text{rf}}/H_p)^4] \times \arcsin(H_p/H_{\text{rf}}) \}. \quad (10)$$

Figure 7 plots  $F(H_{\text{rf}})$  with  $H_p \equiv 50$  Oe. For comparison, two quadratic curves  $\propto H_{\text{rf}}^2$  and  $\propto (H_{\text{rf}} - H_p)^2$  are shown to emphasize the nonquadratic behavior of  $F(H_{\text{rf}})$  around  $H_p$ .

### V. COMPARISON BETWEEN MODEL AND EXPERIMENT

At each temperature and frequency,  $R_s^B$  is determined from the experimentally measured  $R_s$  in the following manner. The low-field  $R_s(H_{\text{rf}})$  is fit to Eq. (1),

$$R_s(H_{\text{rf}}) = R_s^M(H_{\text{rf}}) = R_s(0)[1 + b_R H_{\text{rf}}^2],$$

in the low- and intermediate-field regime. In the high-field regime,  $R_s^B(H_{\text{rf}}) \equiv R_s(H_{\text{rf}}) - R_s^M(H_{\text{rf}})$  with  $R_s^M(H_{\text{rf}})$  the extrapolated values of  $R_s$  from the low- and intermediate-field regime. The extracted  $R_s^B$ , in other

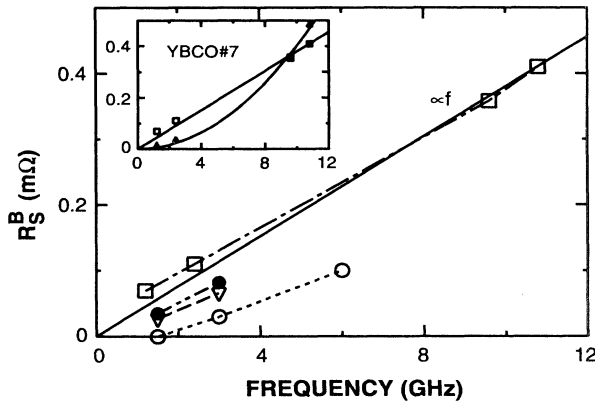


FIG. 8. The frequency dependence of the surface resistance  $R_s^B \equiv R_s - R_s^M$  where  $R_s$  is the measured total surface resistance and  $R_s^M$  the extrapolated value of the  $H_{\text{rf}}^2$ -dependent  $R_s$  from the low- and intermediate-field region. The extracted  $R_s^B$  is attributed to hysteretic losses (see text). For each YBCO sample, the temperature and the rf-field value at which  $R_s^B$  is extracted are given: sample 1 (○) at 79 K and 68 Oe, sample 5 (inverted triangles) at 6.0 K and 500 Oe, sample 6 (●) at 4.3 K and 500 Oe, and sample 7 (□) at 77 K and 120 Oe. For most of the samples,  $R_s^B \propto f^\alpha$  where  $\alpha$  approaches 1, as expected for hysteretic losses [Eq. (8)]. The solid line is the best least-squares linear fit to  $R_s^B$  of sample 7. The inset also plots  $R_s$  (Δ) at very low field and  $R_s^B$  (□) at high rf field versus  $f$ .  $R_s$  for sample 7 exhibits clear  $f^2$  dependence, as expected from the power-dependent coupled-grain model (Ref. 1). In contrast,  $R_s$  for sample 7 shows a linear dependence on  $f$ . The solid lines in the inset are the best least-squares linear and quadratic fits to the low-field  $R_s$  and the high-field  $R_s^B$  data, respectively.

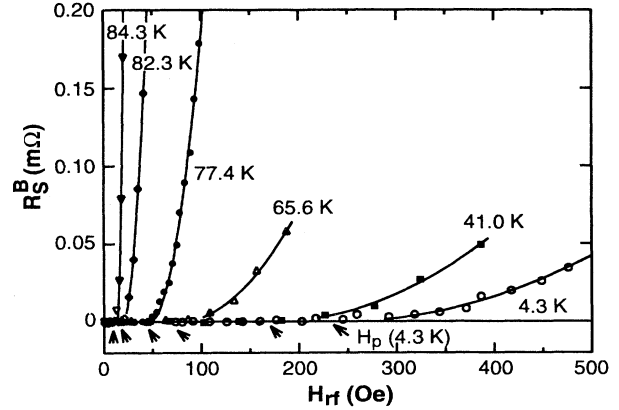


FIG. 9. The  $R_s^B(f, J_c(T), H_p(T)) = R_s - R_s^M$  for sample 1 at several temperatures. The solid lines are fits using a modified Bean critical-state model (see text) with two fitting parameters: the vortex-penetration rf field  $H_p(T)$  and the pinning critical-current density  $J_c^P(T)$ . The  $H_p(T)$  values are indicated at each measurement temperature by the arrows.

words, is simply the deviation from the  $H_{\text{rf}}^2$ -dependent curve.

Figure 8 plots  $R_s^B$  vs  $f$  for several YBCO samples. For each sample,  $R_s^B$  is plotted vs  $f$  at some fixed temperature and rf-field value. For most of the samples,  $R_s^B \propto f^\alpha$  where  $\alpha$  approaches 1, as expected for hysteretic losses [Eq. (8)]. For the other samples, no clear frequency dependence is observed as the data are either lacking or too scattered. The solid line is the best least-squares linear fit  $c_B f^\alpha$ , with the fitting parameter  $c_B$ , to  $R_s^B$  of sample 7. The inset also plots  $R_s$  vs  $f$  at very low rf field for sample 7, which exhibits a clear  $f^2$  dependence, as expected from the power-dependent coupled-grain model.<sup>1</sup> The solid lines in the inset are the best least-squares quadratic and linear fits to the low-field  $R_s$  and the high-field  $R_s^B$  data, respectively.

Figure 9 plots  $R_s^B$  vs  $H_{\text{rf}}$  for sample 1 at  $f = 1.5$  GHz at several temperatures. The solid lines are fits using the hysteretic-loss model developed in the previous section [Eq. (8)] with two fitting parameters: the vortex-penetration field  $H_p(T)$  and the pinning critical-current density  $J_c^P(T)$ . The fits are good over the whole temperature range. Similarly good fits are also obtained for other YBCO films.

#### A. Vortex-penetration field $H_p(T)$

The  $H_p(T)$  values for YBCO from the hysteretic model are about 30% less than the values estimated by eye in both the  $\Delta R_s$  vs  $\lambda$  and the  $\Delta R_s$  vs  $H_{\text{rf}}^2$  plots (e.g., Figs. 3 and 2). These differences between the  $H_p(T)$  values obtained from the fits to the hysteretic model and the eye-detected values arise probably because the method of determining  $H_p$  by detecting a *slight* deviation from the straight lines has large uncertainties. In NbN films where the initial deviation from the  $H_{\text{rf}}^2$  curve is much larger (see Fig. 4), the  $H_p$  values obtained by fitting and

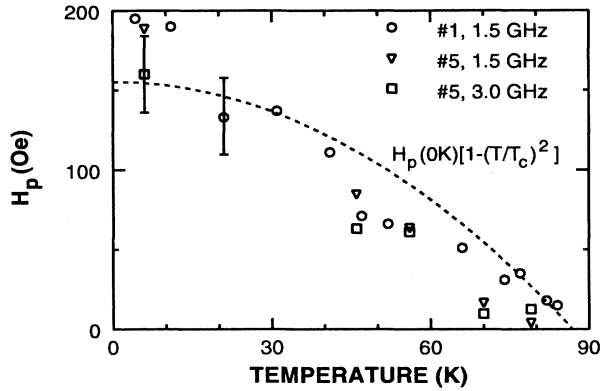


FIG. 10. The fitting parameter  $H_p(T)$ , which is the rf-vortex-penetration field, plotted vs temperature for resonators 1 and 5. For sample 5, results for the first two modes at 1.5 GHz and 3.0 GHz are shown. The dotted line is the best fit to the function  $H_p(T) = H_p(0)[1 - (T/T_c)^2]$  for sample 1 with  $H_p(0)$  a fitting parameter.

the values estimated by eye agree to better than 15% (Fig. 4). Figure 10 shows the temperature dependence of the fitting parameter  $H_p(T)$  for YBCO sample 1 and sample 5. For sample 5,  $H_p(T)$  is approximately the same for both mode 1 (1.5 GHz) and mode 2 (3.0 GHz) over the whole temperature range below  $T_c$ .

Figure 11 shows the frequency dependence of  $H_p$ . For most of the YBCO films, the values of  $H_p(T)$  appear to be independent of frequency for the frequency range considered ( $< 14$  GHz). For some of the samples, which are not shown in Fig. 11,  $H_p$  as a function of frequency exhibits a large amount of scatter that is probably the result of the film's nonuniformity. For different resonant modes, the peaks of the resonant standing waves are located at different places along the length of the stripline. For nonuniform films, the field values for vortex penetration may be different at different locations of the films,

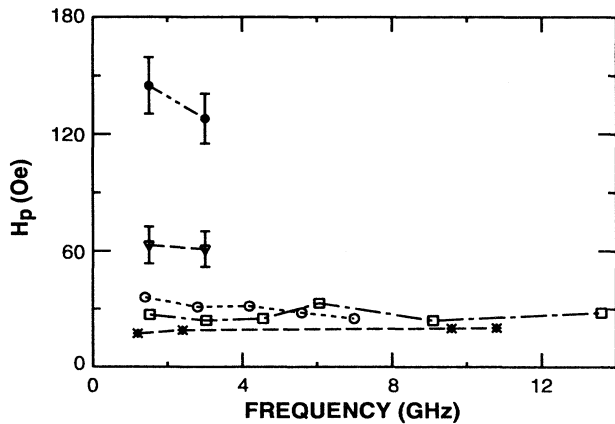


FIG. 11. The fitting parameter  $H_p(T)$  vs resonant frequency for several samples at various temperatures: sample 1 ( $\circ$ ) at 79 K, sample 3 ( $\square$ ) at 78 K, sample 5 ( $\nabla$ ) at 56 K, sample 6 ( $\bullet$ ) at 4.3 K, and sample 7 ( $*$ ) at 77 K. The scatter of the  $H_p(T)$  values is probably the result of the films' nonuniformity (see text).

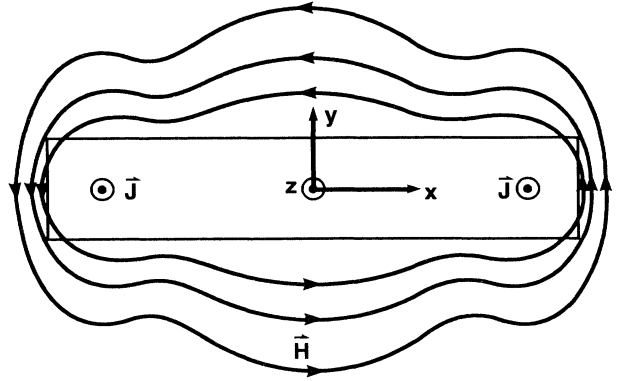


FIG. 12. Schematic showing the current-induced rf magnetic field around the cross-sectional area of a superconducting strip in the Meissner state carrying a rf current (out of the page). The rf magnetic field lines are strongly curved, especially around the edges. Though some field lines penetrate the thin strip, no vortices are formed yet at sufficiently low magnetic field. The field contour lines bulge at the two ends where the current density is highest.

which would lead to different  $H_p$  values for different resonant modes.

The values of  $H_p(T)$  obtained here are lower than  $H_{c1}^{\perp c}$  which are already much lower than  $H_{c1}^{\parallel c}$ , where  $H_{c1}^{\perp c}$  ( $\sim 250$  Oe at 0 K) and  $H_{c1}^{\parallel c}$  ( $\sim 850$  Oe at 0 K) are the lower critical field values measured in YBCO single crystal<sup>3</sup> and epitaxial films<sup>29,30</sup> with an applied dc magnetic field perpendicular and parallel to the  $c$  axis, respectively. Using the anisotropic Ginzburg-Landau model, Klemm<sup>31</sup> calculates the lower critical field  $H_{c1}(\theta_H)$  where  $\theta_H$  is the angle between the  $c$  axis and the dc applied field. He finds that  $H_{c1}(\theta_H)$  decreases rapidly for  $\theta_H > 10^\circ$ . The decrease of  $H_{c1}(\theta_H)$  with increasing  $\theta_H$  for YBCO has also been observed experimentally.<sup>32,33</sup> That our  $H_p$  values reflect  $H_{c1}^{\perp c}$  more than  $H_{c1}^{\parallel c}$  can be attributed to the high curvature of the stripline's rf-field lines, especially around the edges (Fig. 12). For a YBCO film of thickness  $0.3 \mu\text{m}$  and  $\lambda(T) = 0.2 \mu\text{m}$ , the maximum magnetic field at the corners of the center strip with cross section  $0.2 \mu\text{m} \times 150 \mu\text{m}$  makes an angle  $\theta_H \simeq 20^\circ$  with the  $c$  axis.<sup>34</sup>

Since the penetration field  $H_p$  for a YBCO  $c$ -axis film is suppressed towards  $H_{c1}^{\perp c}$  values by the average field curvature,  $H_p$  is expected to be higher for thicker films which have less average curvature. The thickest YBCO sample 4 (Table I) has an  $H_p$  ( $\simeq 380$  Oe at 36 K and  $\simeq 102$  Oe at 77 K) about 3 times larger than those of thinner YBCO films, in agreement with the simple picture of field curvature.

That the  $H_p(T)$  values for YBCO thin films obtained are low even when compared with the intrinsic  $H_{c1}^{\perp c}$  of YBCO single crystals<sup>3</sup> can also be attributed to lower vortex-penetration fields for the junction defects and grain boundaries in the films where vortices first penetrate. Thus, in YBCO thin films, both the strong field curvature and defects and grain boundaries may be working together to lower the  $H_p(T)$  values.

### B. Pinning critical-current density $J_c^P(T)$

Figure 13 plots the second fitting parameter  $J_c^P(T)$  from the modified Bean model for samples 1 and 5. Despite the simplicity of the Bean model, values of the fitting parameter  $J_c^P(T)$  for sample 1 are comparable both in amplitude and temperature dependence with the critical-current density  $J_c^T$  obtained by dc transport measurement on a film deposited under exactly the same conditions. ( $J_c^T$  cannot be measured in the sample 1 used for the resonator, but  $J_c^T$  is available for a sample deposited under the same conditions and this is shown in Fig. 13.) For sample 5, the  $J_c^P(T)$  values extracted for two different modes (mode 1 at 1.5 GHz and mode 2 at 3.0 GHz) are nearly identical.

The  $J_c^P(T)$  values are about an order of magnitude larger than the fitting parameter  $J_c(T)$  extracted from the fits using the power-dependent coupled-grain model in the low- and intermediate-field region<sup>1</sup> for the same films. This difference can be explained as follows: The  $J_c(T)$  in the power-dependent coupled-grain model reflects the critical-current density of a resistively shunted Josephson junction, whose temperature dependence follows the Ambegaokar functional form.<sup>1</sup> This  $J_c(T)$  is directly related to the lower critical field of the junction<sup>35</sup> (i.e., the vortex-penetration field) and has nothing to do with vortex pinning. On the other hand,  $J_c^P(T)$  reflects the vortex-pinning strength<sup>25,26</sup> ( $J_c^P \propto U$ ). Vortices start to penetrate for current densities larger than  $J_c$ , but the magnitude of the hysteretic losses is determined by  $J_c^P$ , as shown in Eq. (8). The transport  $J_c^T$  measures the sum of the junction  $J_c$  and the pinning  $J_c^P$ . In the limit of strong pinning,  $J_c^P \gg J_c$  and hence  $J_c^T \simeq J_c^P$ . Our result  $J_c^T \simeq J_c^P \gg J_c$  implies strong vortex pinning for YBCO, consistent with other vortex-pinning measurements which reveal strong pinning forces in YBCO (see, for instance, Wu and Sridhar<sup>3</sup>). In the

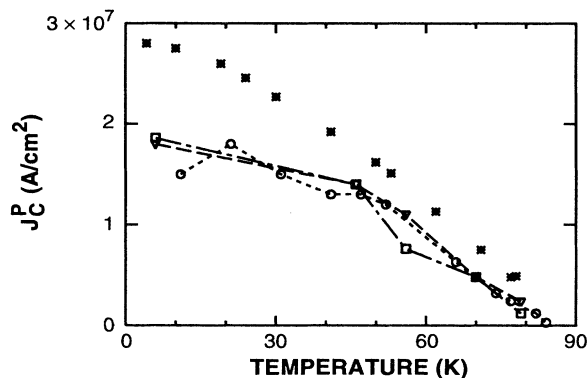


FIG. 13. The fitting parameter  $J_c^P(T)$  which is the pinning critical-current density vs temperature for resonators 1 and 5. The dashed lines are guides to the eye. The first mode for resonator 1 is around 1.5 GHz ( $\circ$ ). For resonator 5, the first two modes at 1.5 GHz ( $\nabla$ ) and 3.0 GHz ( $\square$ ) are shown. The dc critical-current density ( $\boxtimes$ ), as obtained by dc transport measurements on a film deposited under the same conditions as YBCO sample 1, is also shown for comparison.

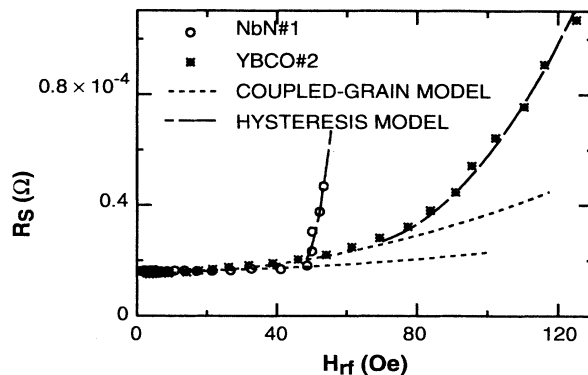


FIG. 14. Comparison between YBCO (asterisks) and NbN ( $\circ$ ) films. The  $R_s$  vs  $H_{rf}$  are plotted for YBCO sample 2 (at 1.5 GHz) and for NbN sample 1 (at 1.7 GHz) at similar reduced temperatures  $T/T_c \simeq 13.4 \text{ K}/15.3 \text{ K} \simeq 78 \text{ K}/90 \text{ K} \simeq 0.87$ . The dotted lines are fits to the power-dependent coupled-grain model (Ref. 1) for the low- and intermediate-rf-field region. The dashed lines are fits to a modified Bean critical-state model.

limit of weak pinning,  $J_c^P \ll J_c$  and hence  $J_c^T \simeq J_c$ . Since the NbN films are highly granular as observed via transmission electron microscopy (with average grain size of about  $0.02 \mu\text{m}$ ), we expect weak pinning for Josephson vortices moving along each junction, because the order parameter is suppressed there.<sup>36</sup> For NbN sample 1 at 13.4 K (Fig. 14), the effective critical-current density of the junction is  $J_c \simeq 5.8 \times 10^5 \text{ A/cm}^2$ , as obtained from the fit using the power-dependent coupled-grain model<sup>1</sup> for the low- and intermediate-rf-field regime, whereas the pinning  $J_c^P$  is  $J_c^P \simeq 1.2 \times 10^5 \text{ A/cm}^2$ , as obtained from the fit using our hysteretic-loss model [Eq. (8)]. These are to be compared with the measured dc transport  $J_c^T$  values of  $0.7$  to  $6.7 \times 10^5 \text{ A/cm}^2$  at 13.4 K for several granular NbN films.

The fact that  $J_c \gg J_c^P$  for NbN compared with  $J_c \ll J_c^P$  for YBCO gives rise to the abrupt change in the  $R_s$  and  $\lambda$  vs  $H_{rf}$  curves for NbN films at  $H_p$ , but only a gradual change for YBCO films. To see more clearly how the abrupt change in NbN comes about, consider the limit of *zero* vortex pinning: As soon as the induced field exceeds the vortex-penetration field  $H_p$  of the film, vortices would penetrate the sample *everywhere*, in the absence of macroscopic shielding current arising from pinning. This sudden influx of vortices would produce sharp changes in the pair density and in the losses, and hence in  $\lambda$  and  $R_s$ , respectively.

## VI. CONCLUSION

We have measured the microwave surface impedance as a function of the microwave magnetic field at various temperatures and frequencies for several types of YBCO films of different thicknesses and for NbN films. For both YBCO and NbN,  $R_s(H_{rf})$  and  $\lambda(H_{rf})$  can be divided into two regions: (1) the low- and intermediate-rf-field

region and (2) the high-rf-field region. The value of  $H_{rf}$  that separates the two regions is the vortex-penetration field  $H_p(T)$ . In the low- and intermediate-field region, the power-dependent coupled-grain model (for the Meissner state) quantitatively accounts for the power dependence of both YBCO and NbN films, giving  $R_s \propto f^2$  and  $\Delta R_s \propto H_{rf}^2$ .

In the high-field region, both  $R_s(H_{rf})$  and  $\lambda(H_{rf})$  deviate from the low-field quadratic dependence on  $H_{rf}^2$ . Using a modified Bean model ( $H_p > 0$ ), we adapted Norris's calculations to account quantitatively for the behavior of  $R_s^B(H_{rf})$  for most YBCO and NbN films at various temperatures and frequencies with two fitting parameters  $H_p(T)$  and  $J_c^P(T)$ . The measured  $R_s^B$  is found to be nearly proportional to frequency for several samples. While we think we have strong evidence that  $R_s^B \propto f$ , some samples did not show a clearly defined frequency dependence, probably because of film nonuniformity as discussed in Sec. V A. The frequency dependence of  $R_s^B$  hence requires further study to understand the effect of nonuniformity.

The values of  $H_p(T)$  obtained show vortex penetration occurring at field values lower than the dc  $H_{c1}^{\perp c}$  values which are already much lower than the dc  $H_{c1}^{\parallel c}$  values. This behavior of  $H_p(T)$  can be explained by the curvature of the magnetic fields at the edge of a superconducting thin-film strip. That the  $H_p(T)$  values obtained for YBCO thin films are low even when compared with the intrinsic  $H_{c1}^{\perp c}$  of YBCO single crystals<sup>3</sup> may be attributed to lower vortex-penetration fields for the junction defects and grain boundaries in the films where vortices first penetrate. The field  $H_p$  is therefore an extrinsic quantity, leaving room for improvement of the power-handling capability of the films through improved deposition techniques.

The values of  $J_c^P(T)$  extracted from the fits using the hysteretic-loss model agree with the critical-current densities  $J_c^T(T)$  obtained by dc transport measurements for YBCO but not NbN films. The disagreement for NbN can be explained by considering the effects of strong vs weak pinning on the  $J_c^T$  values. The strong pinning in YBCO and the weak pinning in NbN also are shown to be responsible for the qualitatively different behavior in  $R_s$  above  $H_p$ .

#### ACKNOWLEDGMENTS

At MIT Lincoln Laboratory, the work was supported by the Advanced Research Projects Agency under the auspices of the Consortium for Superconducting Electronics. The work at the Rome Laboratory was sponsored by the Air Force Office of Scientific Research. We wish to give special thanks to R. P. Konieczka for help with resonator assembly and D. Baker for photolithography. We thank G. Fitch for programming and Dr. R. H. Ono for supplying YBCO sample 6. We also gratefully acknowledge numerous discussions with and suggestions from Professor S. Sridhar and Dr. J. Halbritter. We also would like to thank Professor J. R. Clem and Professor M. Tinkham, and Dr. J. Steinbeck, Dr.

B. A. Willemsen, Dr. J. Derov, and Dr. T. C. L. G. Sollner for useful technical discussions.

#### APPENDIX

##### Field at edges of normal conducting media

To address the magnetic field strength at the edges of a strip, we first review the case of a nonsuperconducting wedge surrounded by a homogeneous dielectric medium with a common straight edge. Figure 15 shows the cross section (perpendicular to the edge) in cylindrical coordinates  $(\rho, \phi, z)$  where  $\epsilon_a, \mu_a$ , and  $\sigma_a = \sigma_{a,1} + j\sigma_{a,2}$  are the permittivity, permeability, and complex conductivity, respectively, of the conducting wedge, while  $\epsilon_b$  and  $\mu_b$  are the permittivity and permeability of the surrounding dielectric medium. We consider only the lossless dielectric medium situation with real  $\epsilon_a, \epsilon_b, \mu_a$ , and  $\mu_b$ .

For  $\sigma_{a,1} = \infty$  (perfect conductivity), using the edge condition that the electromagnetic energy density must be integrable over any finite domain, Meixner<sup>37</sup> studied the singularity of the electric and magnetic fields in the neighborhood of the common edge of angular dielectric or conducting regions at frequencies ranging from dc to microwave. He found that the magnetic field components  $H_\rho$  and  $H_\phi \rightarrow \infty$  at the edge ( $\rho \rightarrow 0$ ) for a sharp wedge ( $\phi_0 > \pi$ ) or an infinitely thin film ( $\phi_0 = 2\pi$ ).

Extending Meixner's approach to the case  $\sigma_{a,1} < \infty$  (lossy conductivity), Geisel *et al.*<sup>38</sup> discovered that  $H_\rho$  and  $H_\phi$  remain bounded unless the media have different magnetic permeabilities<sup>38</sup> ( $\mu_a \neq \mu_b$ ).

The field component parallel to the wedge  $H_z$  is bounded in all the above cases.<sup>37,38</sup>

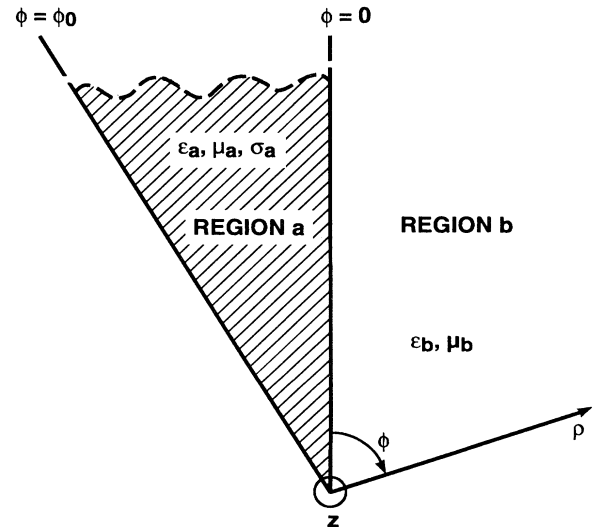


FIG. 15. Cross section of an infinitely long conducting wedge with complex conductivity  $\sigma_a = \sigma_{a,1} - j\sigma_{a,2}$  surrounded by a lossy dielectric medium. For a normal conductor, the imaginary part  $\sigma_{a,2}$  is neglected at low enough frequencies  $f$  (typically,  $f < 10^{11}$  Hz).

### Field at edges of superconducting media

From the two-fluid model, the complex conductivity for the superconductor (region  $a$  in Fig. 15) is  $\sigma_a = \sigma_{a,1} - j\sigma_{a,2}$  where  $\sigma_{a,1} = n_n e^2 \tau / m$  for low enough frequencies  $f$  (typically for  $f < 10^{11}$  Hz) (Ref. 39) where  $n_n$  and  $m$  are the density and mass of the normal carriers,  $e$  the electronic charge, and  $\tau$  the scattering time. An effective complex permittivity can then be written  $\epsilon_a = (\epsilon_a - \sigma_{a,2}) - j\sigma_{a,1} / 2\pi f$ . For  $n_n > 0$  (at nonzero temperature), the superconducting wedge thus behaves like a lossy conductor of finite conductivity  $\sigma_{a,1} < \infty$ , assuming  $\mu_b = \mu_0$ . Note that we have taken  $\mu_a = \mu_b = \mu_0$  since we have treated the superconductor as a nonmagnetic material, with the induced magnetization accounted for by the shielding supercurrent.<sup>40</sup> Thus the magnetic field amplitude at the edges is bounded just as it would be for a lossy normal conducting wedge. This is the case of

interest in this paper.

For  $n_n = 0$  (at zero temperature assuming all carriers become paired), the superconducting wedge can be treated as a lossless ( $\sigma_{a,1} = 0$ ) dielectric instead of conducting wedge. For a right-angle dielectric wedge ( $\phi_0 = 3\pi/2$ ), the magnetic field at the edges is also found to be bounded.<sup>41</sup>

The magnetic field at the edges of a superconducting wedge or thin films is thus finite, at least at temperatures greater than 0. In fact, the current and field distributions in the Meissner state can be *exactly* solved using the London and Maxwell equations numerically. Sheen *et al.*<sup>21</sup> divided the stripline cross section into many small grids and numerically calculated the current and field in each grid. By observing the saturating currents and fields in the grids at the corners and edges as the grid size is continually decreased, they concluded that these currents and fields remain finite at all times.<sup>21</sup>

- <sup>1</sup> P. P. Nguyen, D. E. Oates, G. Dresselhaus, and M. S. Dresselhaus, Phys. Rev. B **48**, 6400 (1993).
- <sup>2</sup> Zhengxiang Ma, R. C. Taber, L. W. Lombardo, A. Kapitulin, M. R. Beasley, P. Merchant, C. B. Eom, S. Y. Hou, and J. M. Phillips, Phys. Rev. Lett. **71**, 781 (1993).
- <sup>3</sup> Dong-Ho Wu and S. Sridhar, Phys. Rev. Lett. **65**, 2074 (1990).
- <sup>4</sup> S. Sridhar, Dong-Ho Wu, and W. Kennedy, Phys. Rev. Lett. **63**, 1873 (1989).
- <sup>5</sup> D. E. Oates, P. P. Nguyen, G. Dresselhaus, M. S. Dresselhaus, C. W. Lam, and S. M. Ali, J. Supercond. **5**, 361 (1992).
- <sup>6</sup> W. Rauch, E. Gornik, G. Sölkner, A. A. Valenzuela, F. Fox, and H. Behner, J. Appl. Phys. **73**, 1866 (1993).
- <sup>7</sup> J. R. Delayen and C. L. Bohn, Phys. Rev. B **40**, 5151 (1989).
- <sup>8</sup> T. L. Hylton, Ph.D. thesis, Stanford University, 1991.
- <sup>9</sup> T. L. Hylton and M. R. Beasley, Phys. Rev. B **39**, 9042 (1989).
- <sup>10</sup> C. Attanasio, L. Mariato, and R. Vaglio, Phys. Rev. B **43**, 6128 (1991).
- <sup>11</sup> A. M. Portis, J. Supercond. **5**, 319 (1992).
- <sup>12</sup> D. E. Oates, W. G. Lyons, and A. C. Anderson (unpublished).
- <sup>13</sup> A. S. Westerheim, L. S. Yu-Jahnes, and A. C. Anderson, IEEE Trans. Magn. **MAG-27**, 1001 (1991).
- <sup>14</sup> A. C. Anderson (unpublished).
- <sup>15</sup> R. H. Ono, J. A. Beall, M. W. Cromar, T. E. Harvey, M. E. Johansson, C. D. Reintsema, and D. A. Rudman, Appl. Phys. Lett. **59**, 1126 (1991).
- <sup>16</sup> H. Piel, H. Chaloupka, and G. Müller, in *Advances in Superconductivity IV*, edited by H. Hagakawa and N. Koshigaki (Springer-Verlag, Tokyo, 1992), p. 925.
- <sup>17</sup> A. C. Anderson, D. J. Lichtenwalner, and W. T. Brogan, IEEE Trans. Magn. **MAG-25**, 2084 (1989).
- <sup>18</sup> C. C. Chin, D. E. Oates, G. Dresselhaus, and M. S. Dresselhaus, Phys. Rev. B **45**, 4788 (1992).
- <sup>19</sup> D. E. Oates, Alfredo C. Anderson, C. C. Chin, J. S. Derov, G. Dresselhaus, and M. S. Dresselhaus, Phys. Rev. B **43**, 7655 (1991).
- <sup>20</sup> D. E. Oates, A. C. Anderson, D. M. Sheen, and S. M. Ali, IEEE Trans. Microwave Theory Tech. **MTT-39**, 1522 (1991).
- <sup>21</sup> D. M. Sheen, S. M. Ali, D. E. Oates, R. S. Withers, and J. A. Kong, IEEE Trans. Appl. Supercond. **AS-1**, 108 (1991).
- <sup>22</sup> W. A. Fietz, M. R. Beasley, J. Silcox, and W. W. Webb, Phys. Rev. **136**, A335 (1964).
- <sup>23</sup> W. I. Dunn and P. Hlawiczka, Br. J. Appl. Phys. (J. Phys. D) **1**, 1469 (1968).
- <sup>24</sup> W. T. Norris, J. Phys. D **3**, 489 (1970).
- <sup>25</sup> P. P. Nguyen, Z. H. Wang, A. M. Rao, M. S. Dresselhaus, J. S. Moodera, G. Dresselhaus, H. B. Radousky, and R. S. Glass, Phys. Rev. B **48**, 1148 (1993).
- <sup>26</sup> T. T. M. Palstra, B. Batlogg, R. B. van Dover, L. F. Schneemeyer, and J. V. Waszczak, Phys. Rev. B **41**, 6621 (1990).
- <sup>27</sup> J. R. Clem, J. Appl. Phys. **50**, 3518 (1979).
- <sup>28</sup> E. H. Brandt and M. Indenbom, Phys. Rev. B **48**, 12893 (1993).
- <sup>29</sup> Ch. Heinzl, Ch. Neumann, Th. Ritzi, and P. Ziemann, J. Supercond. **5**, 319 (1992).
- <sup>30</sup> D. C. Bullock, T. J. Folkerts, P. Klavins, and R. N. Shelton, Physica C **162-164**, 331 (1989).
- <sup>31</sup> R. A. Klemm, Phys. Rev. B **47**, 14630 (1993).
- <sup>32</sup> S. Senoussi and C. Aguilon, Europhys. Lett. **12**, 273 (1990).
- <sup>33</sup> D. E. Farrell *et al.*, Phys. Rev. Lett. **64**, 1573 (1990).
- <sup>34</sup> C. W. Lam (private communication).
- <sup>35</sup> J. R. Clem, Physica C **153-155**, 50 (1988).
- <sup>36</sup> Y. Yeshurun and A. P. Malozemoff, Phys. Rev. Lett. **60**, 2202 (1988).
- <sup>37</sup> J. Meixner, IEEE Trans. Antennas Propag. **AP-20**, 442 (1972).
- <sup>38</sup> J. Geisel, K.-H. Muth, and W. Heinrich, IEEE Trans. Microwave Theory Tech. **MTT-40**, 158 (1992).
- <sup>39</sup> T. van Duzer and C. W. Turner, *Principles of Superconductive Devices and Circuits* (Elsevier, New York, 1981).
- <sup>40</sup> T. P. Orlando and K. A. Delin, *Foundations of Applied Superconductivity* (Addison-Wesley, Reading, MA, 1991), p. 178.
- <sup>41</sup> M. Bressan and P. Gamba, IEEE Microwave Guided Wave Lett. **4**, 3 (1994).